

# Computational Modelling for Biomedical Imaging Project

## Mapping multi-contrast microstructural MRI of the placenta

Simon Ellershaw

May 21, 2021

### 1 Introduction

The placenta provides a vital link between the fetus and mother during pregnancy. This organ is the sole source of oxygen and nutrients throughout the fetus' development. Yet the placenta remains a largely unstudied area of anatomy [1]. Furthermore, abnormalities in the placenta can lead to a complications in the pregnancy such as pre-eclampsia [2].

Currently the diagnosis and monitoring of such abnormalities is limited to the assessment of the fetal biometry and heart rate, amniotic fluid volume and the blood flow in the umbilical cord and arteries using Doppler ultrasound [3]. However, it has been shown that at the time of diagnosis, using these techniques, significant damage to the placenta and so fetus has already occurred [4].

Therefore the development of non-invasive and in-vivo imaging techniques capable of assessing early placental development is highly desirable. Specifically the ability to measure blood oxygenation and flow through the placenta at the early stages of development is an area of active research.

A promising direction is the combination of  $T2^*$  and diffusion MRI.  $T2^*$  relaxometry models the attenuation of an MRI signal due to the sensitivity of the micro-environment to the echo time (TE). One cause of this sensitivity is the paramagnetic property of red blood cell's hemoglobin. Hence magnitude of the  $T2^*$  parameter can be used as an estimate for the blood oxygenation of the micro-environment [5]. By additionally varying the size of the magnetic b-field the diffusion coefficient  $D$  can be determined. This is a proxy for the fluid flow rate, for example blood flow [6].

For such an approach to be successful the complex structure of the placenta must be accounted for in the fitting of the  $T2^*$  and  $D$  parameters. As shown in Fig.1, a number of different fluids with varying oxygen and flow rates are present in the placenta including fetal and maternal blood and pooled fluid in the intervillous space. These potentially could all contribute an intra-voxel micro-environment or compartment with a specific  $T2^*$  and  $D$  parameters.

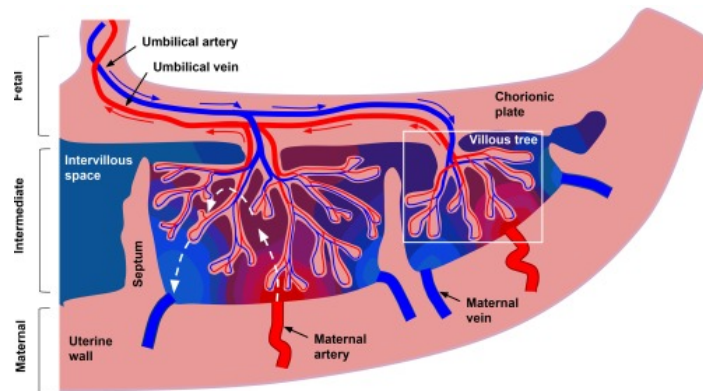


Figure 1: Schematic cross-sectional diagram of the placenta and surrounding tissue [7].

This project therefore fits and evaluates a number of increasingly complex compartment models to a series of MRI scans with varying  $b$  and TE settings. The ability of these models to fit the data along with their biological plausibility is then evaluated. Differences in the model outputs for a healthy and abnormal pre-eclampsia placenta are also analysed.

## 2 Methodology

### 2.1 Data Exploration

This project uses series of retrospective MRI scans taken of two placenta; a healthy control and a pre-eclampsia patient. For each placenta, 330 scans have been taken across a grid of 14 b-values and 5 echo times (TE) as shown in Fig.2. Furthermore there are pre-existing binary masks of each placenta with and without the uterine wall to define the region of interest (ROI) for modelling as shown in Fig.3. In this project the mask including the uterine wall is used exclusively as it gives a more holistic view of the organ.

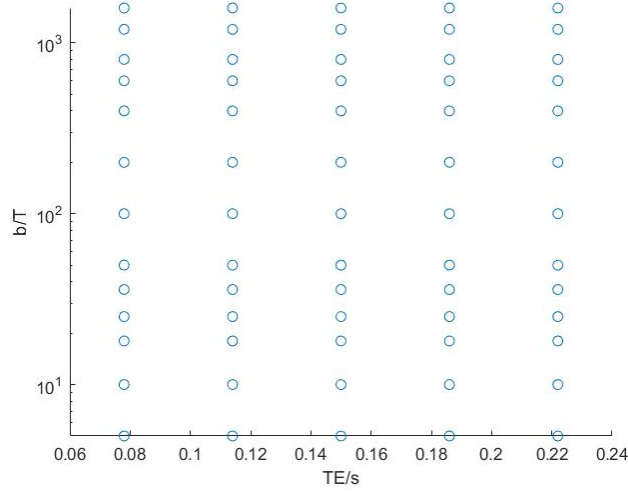


Figure 2: Plot showing the grid of b-values and TE used when collecting the MRI scans used in this project

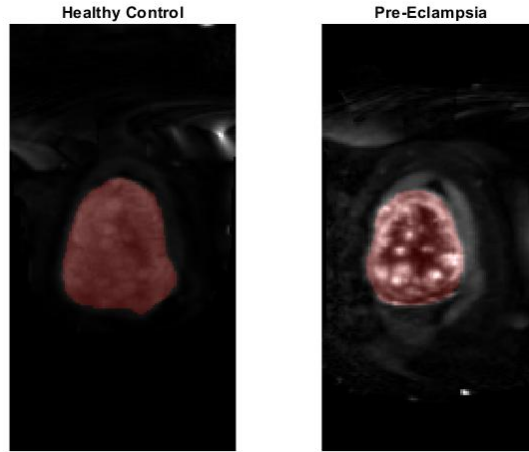


Figure 3: Visualisation of a sample slice of a healthy and a pre-eclampsia scan ( $b = 0T$ ,  $TE=0.078s$ ). The mask of placenta including uterine wall is shown in red.

### 2.2 $T2^*$ -ADC Model

The simplest combined diffusion and  $T2^*$  models assumes each voxel contains a single tissue compartment. Hence the attenuation of the signal due to  $T2^*$  and  $D$  can be modelled as a single exponentials. This gives the  $T2^*$ -ADC model [8],

$$S(T_E, b) = S_0 e^{\frac{-TE}{T_2^*}} e^{-bD}, \quad (1)$$

where  $S_0$  is the unattenuated signal.

The model parameters  $S_0$ ,  $T_E$  and  $ADC$  are fitted voxelwise by gradient descent. Assuming Gaussian noise allows this to be done by minimising the sum of squared errors ( $SSE$ ) between the true,  $S$ , and predicted,  $\hat{S}$ , signals for every pixel and  $b$ - $T_E$  combination,

$$SSE = \sum_{i=1}^n (y_i - \hat{y}_i)^2. \quad (2)$$

Multiple runs, with perturbations to the initial starting parameters, are conducted to avoid fitting to a local minima. The number of runs is decided by running gradient descent on a number of sample voxels 1000 times and calculating the proportion of runs,  $o$ , that contain the minimum found value. From this the number of runs,  $n$ , required to find a minimum in 95% of cases can be calculated as,

$$n = \frac{\ln(0.05)}{\ln(1 - o)}. \quad (3)$$

$n$  has been found to be 2.4 for this model and so 5 runs have been used in the fitting process.

Constraints on the range of possible parameter values are enforced to maintain the biological plausibility of the model fit. This is done through the use of function substitution within the model.  $T_2$  and  $D$  are constrained between 0 and a constant  $C$  by the function  $C \sin^2(x)$ ,  $C_{T_2} = 1$  and  $C_D = 10$ . Whilst  $S_0$  is set to be greater than 0 by the  $x^2$  function.

### 2.3 IVIM Model

The assumption of a single tissue compartment made by the  $T_2^*$ -ADC model runs orthogonal to the complex placenta anatomy shown in Fig.1. Therefore a natural extension is to include an additional compartment as in the intravoxel incoherent motion (IVIM) model [9]. This incorporates the attenuation of the signal due to two compartments with differing fluid flows as,

$$S(T_E, b) = S_0 e^{-\frac{T_E}{T_2^*}} [f e^{-bD_1} + (1 - f) e^{-bD_2}], \quad (4)$$

where  $f$  is the proportion of fluid in the first compartment,  $D_1$  is the diffusion coefficient of the fast moving fluid and  $D_2$  the coefficient of the slow moving fluid. Hence  $D_1 > D_2$ .

The IVIM model has been fitted to both placenta scans using the same gradient descent method as outlined for the  $T_2^*$ -ADC model.  $n$  has been estimated to be 2.7 for this model so again fitting is conducted 5 times for each voxel.  $f$  is constrained between 0 and 1,  $D_1$  between 0 and 10 and  $D_2$  is set to be  $0 < D_2 < D_1$  by the appropriate choice of constant in the function  $C \sin^2(x)$ .

### 2.4 Continuum Model

Both the models outlined in Sections 2.2 and 2.3 explicitly assume the number of signal compartments. However this can be learnt directly from the data through the spectra produced by the continuum model [8].

This model calculates the signal by integrating over all possible  $T_2$  and  $D$  values where the contribution of the parameter combination is determined by the 2D spectra,  $F(T_2^*, D)$ ,

$$\bar{S}(T_E, b) = \int F(T_2^*, D) e^{-\frac{T_E}{T_2^*}} e^{-bD} dT_2^* dD. \quad (5)$$

It is of note that  $\bar{S}$  is the signal averaged across the ROI. By pre-determining the range of  $T_2^*$  and  $D$  to give a 2D grid of  $N_{T_2^*} \times N_D$  values Eqn.5 can be discretised,

$$\bar{S}(T_E, b) = \sum_{i=1}^{N_{T_2^*}} \sum_{j=1}^{N_D} F(T_{2_i}^*, D_j) e^{-\frac{T_E}{T_{2_i}^*}} e^{-bD_j}, \quad (6)$$

where  $(i, j)$  are coordinates on the pre-defined grid. The grid in this project is 50x50 and  $T_2^*$  takes linearly spaced values between 0 and 0.1 whilst  $D$  takes logarithmically spaced values between  $10^{-3}$  and  $10^1$ .

As the exponential decays terms are known for given  $b_k$  and  $TE_k$  values these can be separated into a kernel vector,  $K_k$ . Furthermore, flattening the 2D spectra into a vector,  $F$  of length  $N_{T2} * N_D$  allows Eqn.6 to be written in vector notation for a single scan,  $\bar{S}_k$ , as

$$\bar{S}_k(TE_k, b_k) = K(TE_k, b_k).F. \quad (7)$$

Extending this formulation to include all scans,  $\bar{S}$ , requires simply calculating the kernel function for all sets of  $TE$  and  $b$  values,

$$\bar{S}(TE, b) = K(TE, b).F. \quad (8)$$

$F$  can then be solved for as a non negative least-squares curve fitting problem,

$$\min_F ||K(TE, b).F - \bar{S}(TE, b)||^2, \text{ where } F \geq 0. \quad (9)$$

## 2.5 3-Compartment Model

The results of the Continuum Model, see Section 3.2, indicates the presence of a 3 separate compartments. Therefore the models presented in Section 2.2 and 2.3 are again extended to include a third compartment [10],

$$S(TE, b) = S_0 e^{-\frac{TE}{T2^*}} [f e^{-bD_1} + (1-f)\{v e^{-bD_2} + (1-v) e^{-bD_3}\}]. \quad (10)$$

This is done by including an additional diffusivity attenuation parameter  $D_3$  and proportion parameter  $v$ . Additional  $T2^*$  parameters could be added. However, the continuum spectra, see Fig.6, shows peaks at similar  $T2^*$  values and so the additional parameters are not thought to be required due to the trade-off with model complexity.

The constraints on the D parameters are such that  $D_1 > D_2 > D_3$  and  $v$  is bounded between 0 and 1. The model is fitted using the same gradient descent methodology as outlined for the  $T2^*$ -ADC model.

## 2.6 Model Selection

Finally the  $T2^*$ -ADC, IVIM and 3-Compartment model are compared on the basis of the bayesian information criterion (BIC) [11]. This metric balances the complexity of a model in terms of it's number of parameters,  $N$ , and the likelihood of the model,  $L$ ,

$$BIC = N \log(K) - 2 \log(L), \quad (11)$$

which given the assumption of Gaussian noise and the number of scans taken,  $K$ , gives

$$BIC = (N + 1) \log(K) - K \log(SSE/K). \quad (12)$$

This allows both voxelwise and whole scan comparison of the ability of the 3 models fitted to model the signal based on which minimises the BIC. The continuum model is not assessed as it uses the averaged signal across the scan instead of individual voxels.

# 3 Results

## 3.1 Parameter Maps

Fig.4 visualises the fitted parameters of the three voxelwise model presented in Section 2. The  $S_0$  parameter models the unattenuated signal and so offers little additional insight than that gained from looking at the true signal for a scan with low  $b$  and  $TE$  settings. It is of note that the healthy and pre-eclampsia maps are consistent across the models as expected.

The  $T2^*$  parameter has been treated as a constant across all compartments in each model. Hence the  $T2^*$  parameter maps across the models have a high degree of similarity. All healthy  $T2^*$  maps have regions of high  $T2^*$  encircled by areas of low  $T2^*$ . This matches previously identified patterns [12] and these areas of highly oxygenated blood are likely to correspond to placental lobes. In comparison, the pre-eclampsia patient has similar but less pronounced placental lobe

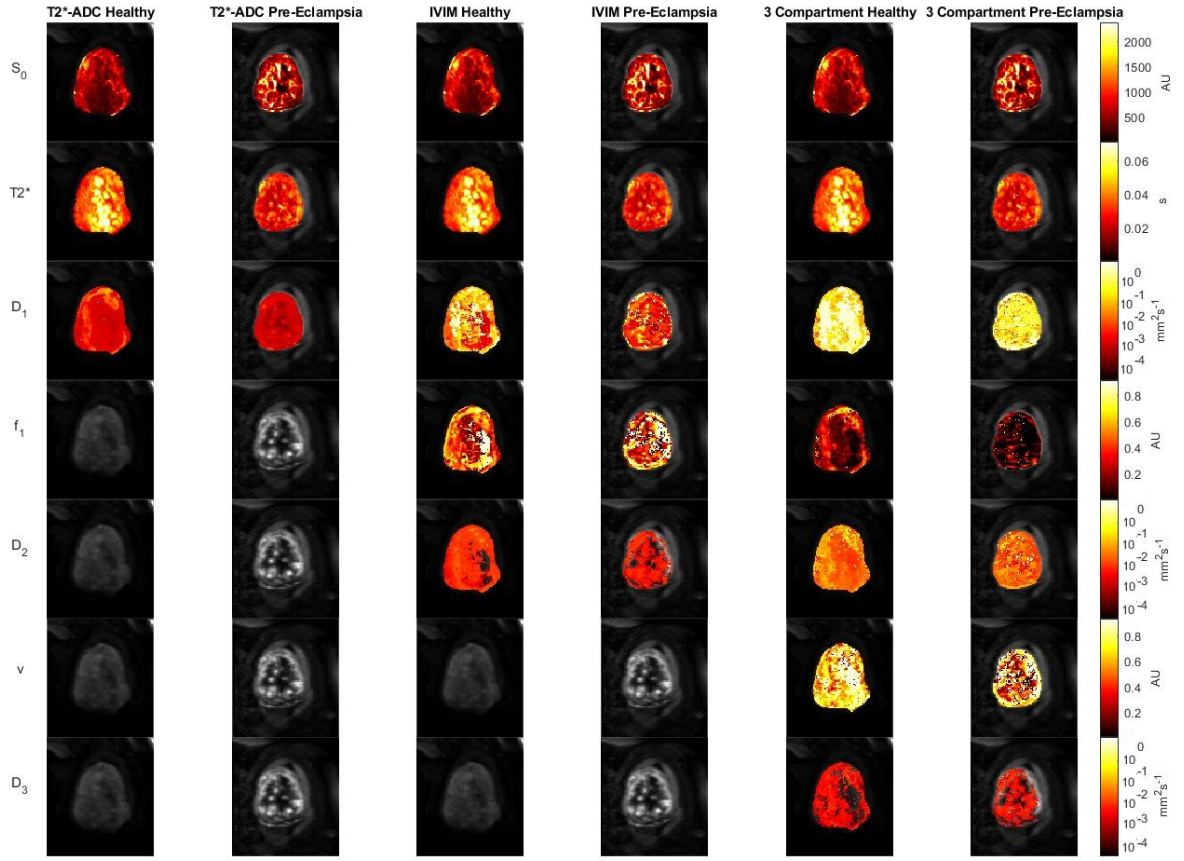


Figure 4: Parameter maps of the T2\*-ADC, IVIM and 3-Compartment models overlaid on sample MRI scan signals. Maps for both the healthy control and pre-eclampsia patient are shown.

features. These maps also show areas of very low T2\* corresponding to areas of low and potential harmful oxygenation levels within the placenta. This phenomena is further evidenced by the downward shift of the T2\* distribution when the T2-ADC model is fitted to the pre-eclampsia scans, see Fig.5.

The healthy  $D_1$  T2-ADC model shows a band of high diffusivity across the left upper side. Anatomically this aligns with the border between the placenta and uterine wall. This is an area of high blood flow and so is anatomically plausible. Furthermore, the  $f_1$  parameter can be interpreted as the fraction of fast moving fluid in the voxel. As  $f_1$  maps for both the IVIM and 3-Compartment model also show a similar uterine wall band this feature is captured by all models. However, in the pre-eclampsia patient this band is not present for any model. For example, in the 3-Compartment model the  $f_1$  map and so proportion of fast moving blood is order of magnitudes lower than it's healthy comparison. This is further shown by the absence of a second high valued peak in the  $D_1$  distribution of the T2-ADC model parameters, see Fig.5.

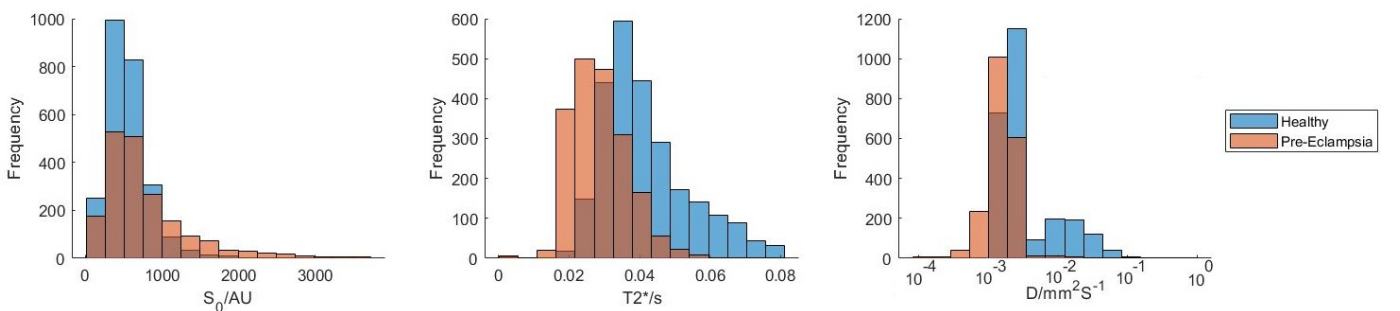


Figure 5: Distribution of the T2-ADC model parameters when fitted to slice 7 of the healthy and pre-eclampsia scans.

A further qualitative discriminative feature are the small islands of relatively high  $D$  surrounded by low  $D$  only present in the pre-eclampsia scans. These are present for the slowest moving fluid tissue and so can be seen in only the lowest  $D$  maps for each model. For example, the IVIM  $D_2$  map clearly shows this feature for the pre-eclampsia patient but not the healthy control.

### 3.2 Continuum Spectra

The spectra from the continuum model, see Fig.6, shows three separate peaks for the healthy control. These peaks are found at  $D$  values of  $3.16 \times 10^{-3}$ ,  $2.51 \times 10^{-2}$  and  $7.94 \text{ mm}^2\text{s}^{-1}$  and an approximately constant  $T_2^*$  value of  $0.045\text{s}$ . These peaks correspond to those found in previous work [8]. The two highest peaks have  $D$  values greater than the approximate diffusivity of water in free media at  $37^\circ\text{C}$  which is  $3 \times 10^{-3} \text{ mm}^2\text{s}^{-1}$  [13]. This suggests the presence of two compartments with differing incoherent flow speeds. Whilst the lowest peak is due to the diffusion of water within tissue. The appearance of the 3 peaks at differing but similar  $T_2^*$  values motivated the 3-Compartment outlined in Section 2.5.

In contrast, for the pre-eclampsia spectra the two high peaks do not appear. Also the lowest peak  $T_2^*$  value is shifted downwards significantly. This agrees with the previous qualitative description the pre-eclampsia parameter maps in Fig.4 where the areas of high  $D$  in the uterine wall were not observed and the  $T_2^*$  maps are significantly lower.

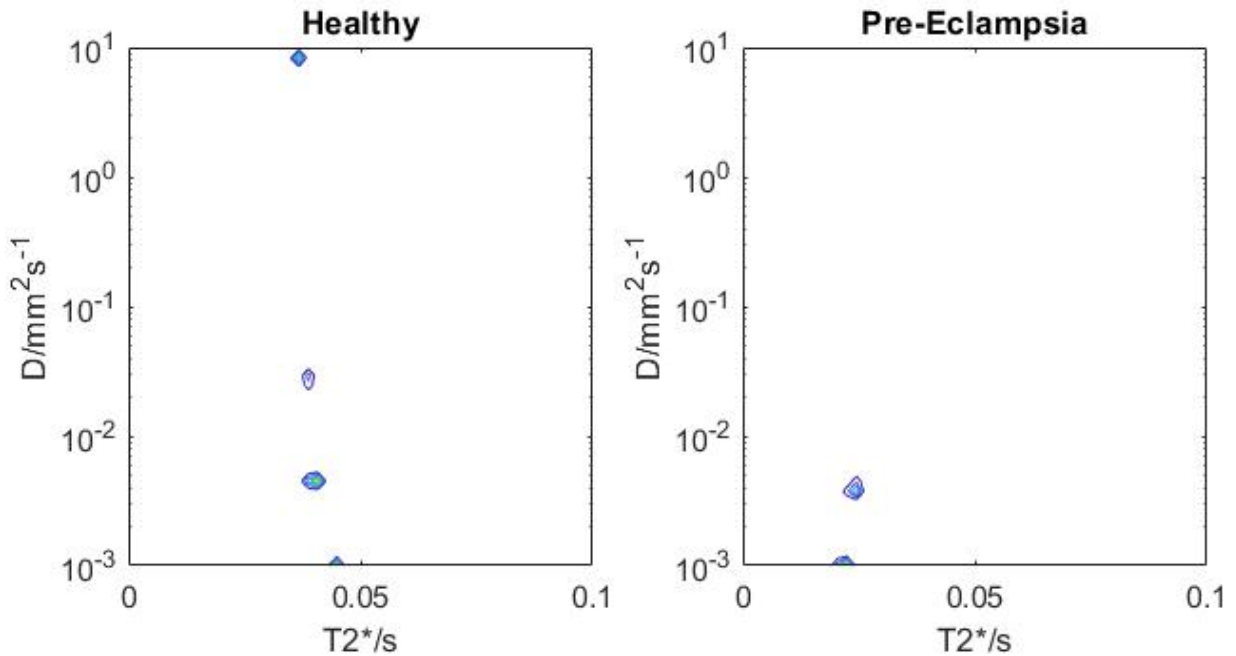


Figure 6: Visualisation of the continuum model spectra when fitted to both the healthy and pre-eclampsia scans.

### 3.3 Model Selection

The final experiment, compares the 3 model's performance, in totality and voxelwise, when fitted to a single slice of MRI scans. The results on a voxelwise basis, see Fig.7, shows that in terms of minimising SSE the 3-Compartment model dominates. However, when analysing the BIC results the picture is mixed. For the healthy control, there is a band on the upper left side in which the 3-Compartment model achieves the minimum BIC. This intersects with the area identified as the uterine wall boundary and so further suggests that this region contains multiple high flow environments. In general though the IVIM model minimises the BIC metric, as shown in Table 1. This suggests the 3-Compartment model could be overfitting the data.

Model	SSE Healthy $\times 10^7$	SSE Pre-Eclampsia $\times 10^7$	BIC Healthy $\times 10^6$	BIC Pre-Eclampsia $\times 10^6$
T2*-ADC	0.64	1.18	0.93	1.61
IVIM	0.59	1.03	0.91	1.58
3-Compartment	0.53	1.06	0.92	1.60

Table 1: The total SSE and BIC for each model when summed over all voxels in slice 7 for both the healthy and pre-eclampsia scans

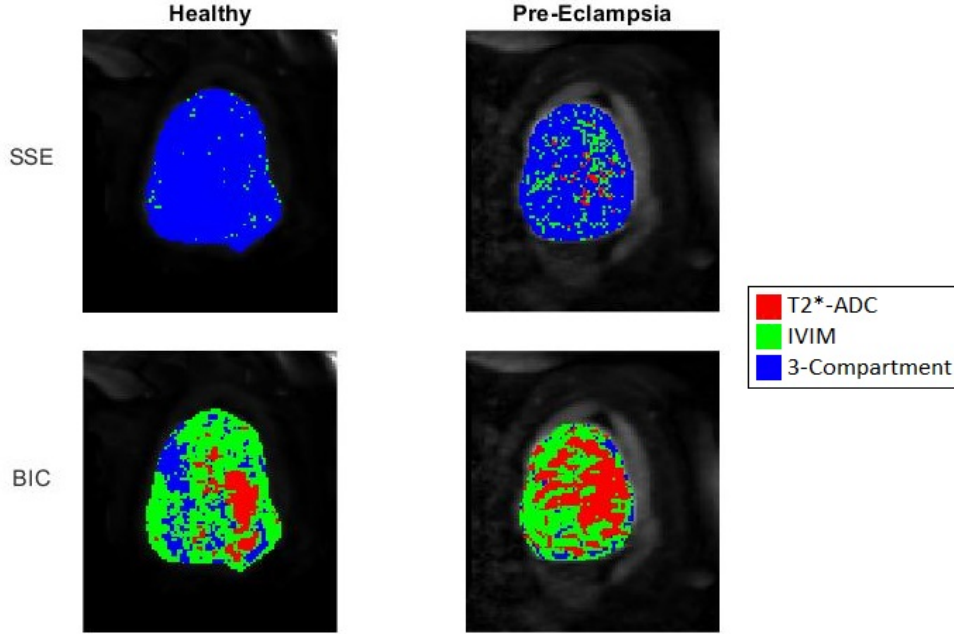


Figure 7: Maps showing the model which minimises the SSE or BIC metric at each voxel of slice 7 of the healthy and pre-eclampsia scans.

## 4 Discussion

The continuum spectra of the healthy scans shown in Fig.6 provides strong evidence that there are three compartments with different diffusivities contained within the placenta. Previous work [8] has provided plausible biological interpretation for these peaks based on dissection of mice placenta [14]. Namely a slow diffusing blood compartment, a fast flowing arterial blood compartment and an intermediate compartment due to the active filtration of fluid across the fetal-maternal barrier. These assignments are consistent with the healthy 3-Compartment maps presented in Fig.4. As previously described the  $f_1$  map has high parameter values in the uterine wall region containing fast flowing maternal blood arteries. The  $D_2$  map shows a general desaturation through the placenta tissue mimicking the fetal maternal barrier. Finally the  $D_3$  map shows plausible areas for maternal blood pooling within the placenta.

Although the spectra provides evidence for the 3-Compartment model further results in this project cast doubt on this modelling assumption. Firstly, in Fig.5 the D plot shows two distinct peaks not three as expected by the 3-Compartment model. Furthermore, the results of the BIC model selection, see Section 3.3, show the IVIM model to minimise this criterion despite the 3-Compartments superior SSE scores. This suggests that the 3-Compartment model may be overfitting the given data.

However, the metrics from this selection process are within 1% of each other and so to draw a statistically significant conclusion from these results would be unwise. Further work to establish the uncertainty on these values through the use of techniques such as bootstrapping or markov chain Monte Carlo (MCMC) would therefore be valuable. However, to determine the truly biologically correct model of the placenta would require the ex vivo histology of a human placenta. This is beyond the scope of this project and so left to future work.



Finally, it is of significance that all the models presented in this work gave the ability to quantitatively discriminate between the healthy and pre-eclampsia scans. The distinct shift of downward shift in  $T2^*$  and  $D$  parameters can be qualitatively seen in the continuum model, Fig.6, and all voxelwise parameter maps in Fig.4. However, this work has not attempted to quantify these differences in a statistically robust test. Furthermore, this project uses a dataset of only two placenta. Therefore, to move the promising results shown here closer to being used in clinical practice these two shortcomings should be addressed in future work.

## 5 Conclusion

This project has evaluated the ability of a 1,2 and 3 compartment model to fit MRI placenta signals when the TE and b settings are varied. Use of a continuum model gives evidence that 3 compartments with distinct  $D$  values are present. However, the decrease in SSE through the use of a 3-Compartment is not large enough to offset the increase in model parameters according to the BIC metric. Further statistical or ex vivo work would be required to prove the 3-Compartment model. Promisingly though all models showed an ability to qualitatively discriminate between healthy and pre-eclampsia scans. However, work to quantify these differences on a larger sample size is required before potential clinical application is possible.

## References

- [1] D Michael Nelson. How the placenta affects your life, from womb to tomb. *American Journal of Obstetrics & Gynecology*, 213(4):S12–S13, 2015.
- [2] Leslie Myatt. Role of placenta in preeclampsia. *Endocrine*, 19(1):103–111, 2002.
- [3] Apostolos Kaponis, Takashi Harada, George Makrydimas, Tomoiki Kiyama, Kazuya Arata, George Adonakis, Vasilis Tsapanos, Tomio Iwabe, Theodoros Stefos, George Decavalas, et al. The importance of venous doppler velocimetry for evaluation of intrauterine growth restriction. *Journal of ultrasound in medicine*, 30(4):529–545, 2011.
- [4] Susan Snyder. Major changes in diagnosis and management of preeclampsia. *Journal of midwifery & women's health*, 59(6):596–605, 2014.
- [5] Jason M Zhao, Chekesha S Clingman, M Johanna Närväinen, Risto A Kauppinen, and Peter CM Van Zijl. Oxygenation and hematocrit dependence of transverse relaxation rates of blood at 3t. *Magnetic Resonance in Medicine: An Official Journal of the International Society for Magnetic Resonance in Medicine*, 58(3):592–597, 2007.
- [6] Sara Sohlberg, Ajlana Mulic-Lutvica, Peter Lindgren, Fransisco Ortiz-Nieto, A-K Wikström, and Johan Wikström. Placental perfusion in normal pregnancy and early and late preeclampsia: a magnetic resonance imaging study. *Placenta*, 35(3):202–206, 2014.
- [7] Paddy J Slator, Jana Hutter, Laura McCabe, Ana Dos Santos Gomes, Anthony N Price, Eleftheria Panagiotaki, Mary A Rutherford, Joseph V Hajnal, and Daniel C Alexander. Placenta microstructure and microcirculation imaging with diffusion mri. *Magnetic resonance in medicine*, 80(2):756–766, 2018.
- [8] Paddy J Slator, Jana Hutter, Marco Palombo, Laurence H Jackson, Alison Ho, Eleftheria Panagiotaki, Lucy C Chappell, Mary A Rutherford, Joseph V Hajnal, and Daniel C Alexander. Combined diffusion-relaxometry mri to identify dysfunction in the human placenta. *Magnetic resonance in medicine*, 82(1):95–106, 2019.
- [9] Denis Le Bihan, Eric Breton, Denis Lallemand, ML Aubin, Jean Vignaud, and M Laval-Jeantet. Separation of diffusion and perfusion in intravoxel incoherent motion mr imaging. *Radiology*, 168(2):497–505, 1988.



- [10] Andrew Melbourne, Rosalind Aughwane, Magdalena Sokolska, David Owen, Giles Kendall, Dimitra Flouri, Alan Bainbridge, David Atkinson, Jan Deprest, Tom Vercauteren, et al. Separating fetal and maternal placenta circulations using multiparametric mri. *Magnetic resonance in medicine*, 81(1):350–361, 2019.
- [11] Shawn Bauldry. Structural equation modeling. In James D. Wright, editor, *International Encyclopedia of the Social & Behavioral Sciences (Second Edition)*, pages 615–620. Elsevier, Oxford, second edition edition, 2015.
- [12] Jana Hutter, Paddy J Slator, Laurence Jackson, Ana Dos Santos Gomes, Alison Ho, Lisa Story, Jonathan O’Muirheartaigh, Rui PAG Teixeira, Lucy C Chappell, Daniel C Alexander, et al. Multi-modal functional mri to explore placental function over gestation. *Magnetic resonance in medicine*, 81(2):1191–1204, 2019.
- [13] Edward Lansing Cussler and Edward Lansing Cussler. *Diffusion: mass transfer in fluid systems*. Cambridge university press, 2009.
- [14] Eddy Solomon, Reut Avni, Ron Hadas, Tal Raz, Joel Richard Garbow, Peter Bendel, Lucio Frydman, and Michal Neeman. Major mouse placental compartments revealed by diffusion-weighted mri, contrast-enhanced mri, and fluorescence imaging. *Proceedings of the National Academy of Sciences*, 111(28):10353–10358, 2014.